Electronic Supplementary Information (ESI)

A powerful approach to functional graphene hybrids for high performance energy-related applications

Chuangang Hu, Guanpei Zheng, Fei Zhao, Huibo Shao, Zhipan Zhang, Nan Chen, Lan Jiang, and Liangti Qu

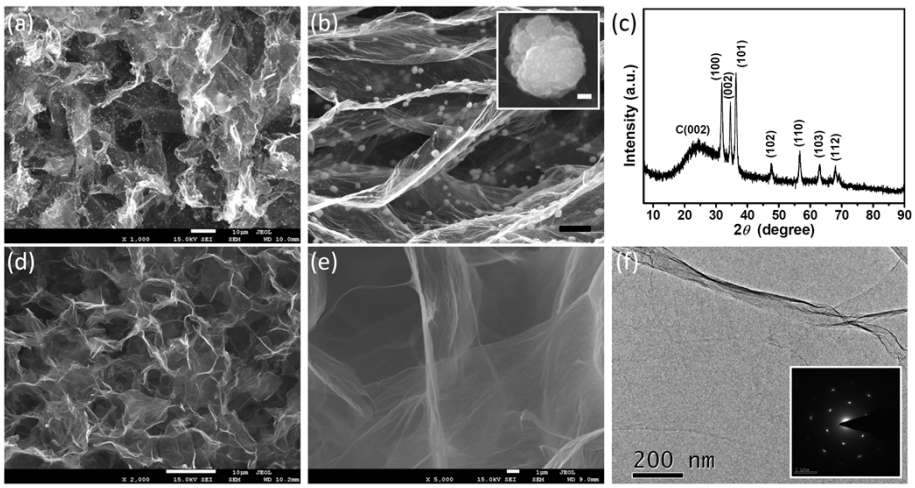

Figure S1. (a, b) SEM images of the as-prepared 3D RGO derived from Zn foil. The inset in (b) is the enlargement image of ZnO nanoparticle. (c) The corresponding XRD pattern. (d, e) SEM images of 3D RGO after the removal of ZnO under different magnifications. (f) TEM image of RGO. The inset in (f) is the electron diffraction of the graphene sheet. Electron diffraction pattern of the RGO sheets presents clear diffraction spots without halation, implying the highly crystalline graphene structure. The scale bars in (b) and the insert in (b) are 1μm and 20 nm, respectively.

SEM images reveal that RGO deposited on Zn foil has a layered structure with ZnO particles (Figure S1a&b), and the XRD pattern (Figure S1c) shows the representative peak of GO ($2\theta \approx 11°$) has completely disappeared in the as-prepared samples, accompanied with a new broad peak centered at around 25° and a series of sharp peak. The broad peak located at $2\theta \approx 25°$ is assigned to the (002) plane of stacked graphene sheets. The peaks at $2\theta \approx 32°$, 34°, 36°, 48°, 57°, 66°, and 68°correspond to the (100), (002), (101), (102), (110), (103), and (112) planes of hexagonal structure of ZnO (JCPDS ICDD card NO. 05-0664). These particles are easily removed by aqueous NaOH (Figure S1d&e) and the electron diffraction pattern presents the clear diffraction spots (Figure S1f), demonstrating the highly crystalline graphene structure. In consistent with the XRD analysis, the electron diffraction pattern indicates the

effective reduction of GO by Zn foil.

Figure S2. Photo of the as-obtained Pt/3DRGO sample.

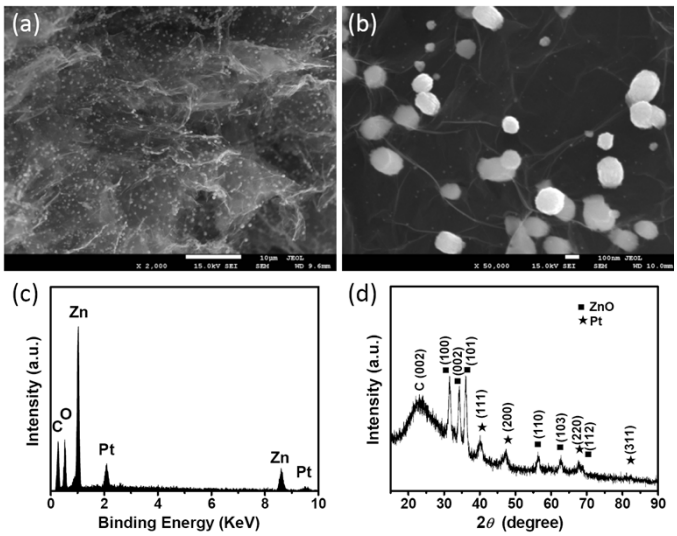

Figure S3. (a, b) SEM images of as-prepared Pt/RGO before treating with NaOH solution. (c) The corresponding EDS spectroscopy. (d) XRD pattern. All the analysis tends to support the conclusion that ZnO particles and small Pt nanoparticles are coexisted in the as-prepared sample.

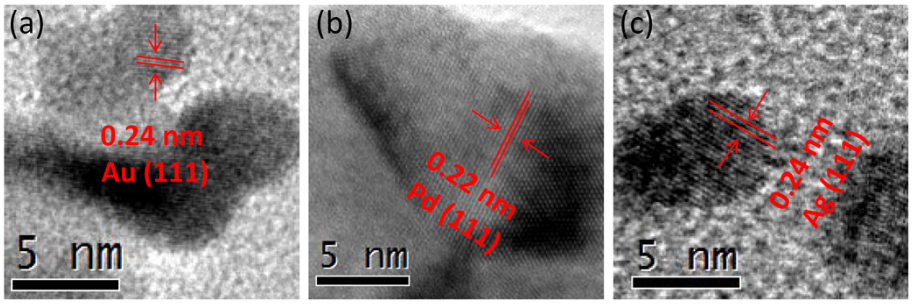

Figure S4. HR-TEM images of the 3D graphene supported Au, Pd, Ag nanocrystallines. The interplanar spacing displayed in the images indicates the formation of the corresponding metals on the graphene.

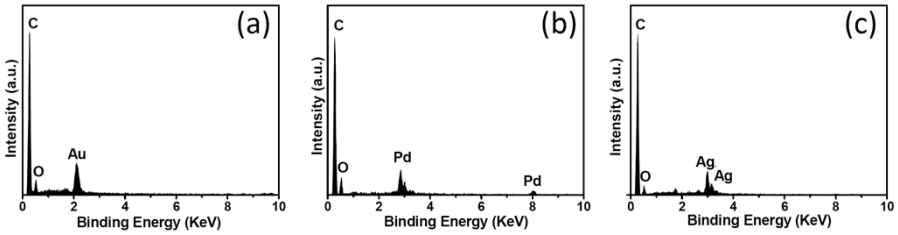

Figure S5. (a–c) EDSs of Au/RGO, Pd/RGO and Ag/RGO, respectively.

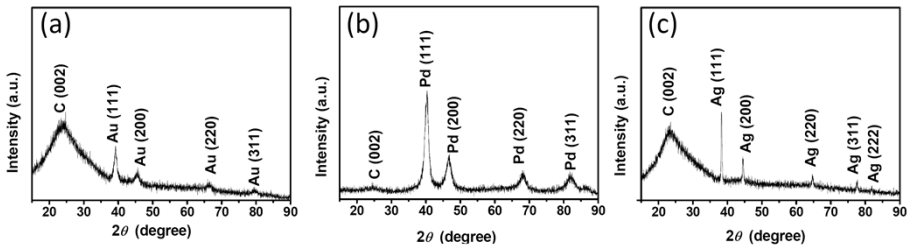

Figure S6. XRD patterns of Au/RGO, Ag/RGO and Pd/RGO, respectively.

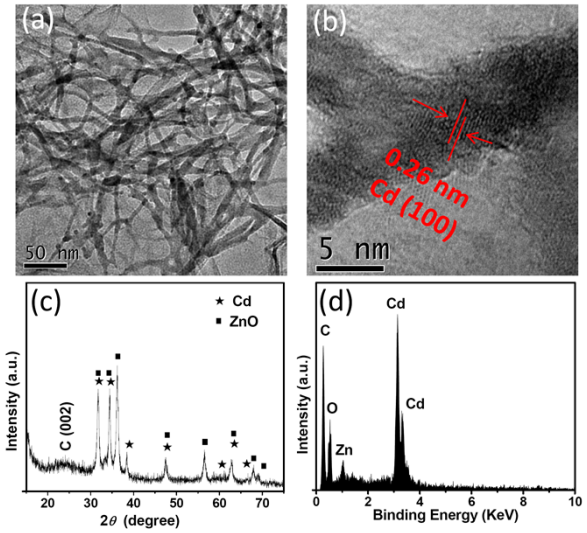

Figure S7. (a, b) HR-TEM images of the 3D graphene supported Cd nanocrystallines under different magnifications. The interplanar spacing displayed in the images indicates the formation of Cd nanowires on the graphene. (c) EDS of Cd/RGO. (d) XRD pattern of Cd/RGO.

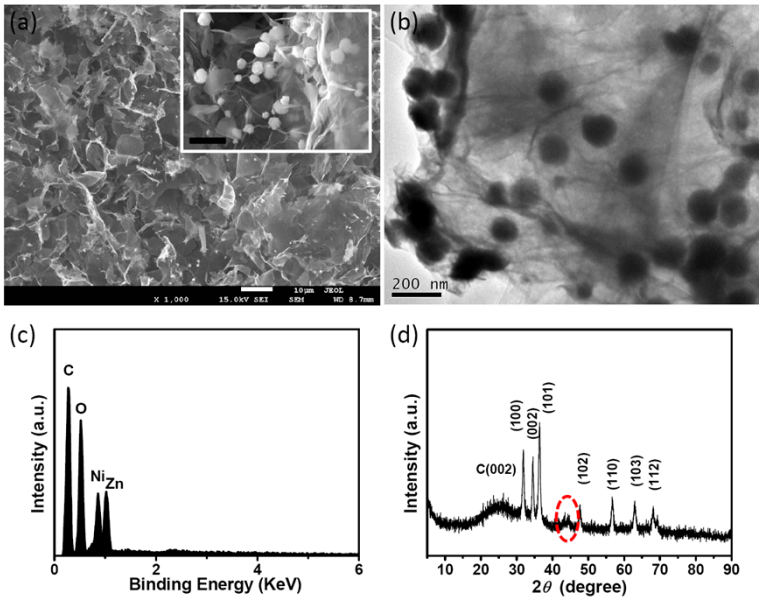

Figure S8. (a, b) SEM and TEM images of the as-prepared RGO@NiO/Ni before treating with NaOH solution, and the inset in (a) is the enlargement image of ZnO nanoparticle. (c) The corresponding EDS spectroscopy. (d) XRD pattern. The scale bar in the insert in (b) is 1μm.

The as-prepared RGO@NiO/Ni sample that NiO/Ni functionalized 3D network of RGO sheets on the Zn foil was shown in Figure S8. SEM and TEM images illustrate the existence of ZnO particles in the as-prepared sample. The XRD pattern shows the peaks at 2θ ≈ 32°, 34°, 36°, 48°, 57°, 63°, 66°, and 68° correspond to the (100), (200), (101), (102), (110), (103), (200), and (112) planes of hexagonal structure of ZnO (JCPDS ICDD card NO. 05-0664), accompanied with a broad peak centered at around 25° assigned to the (002) plane of stacked RGO sheets. Furthermore, the representative weak peaks of NiO and Ni (ca. 43° and 44°) indicate the formation of relative low crystallinity of NiO and Ni hybrids.

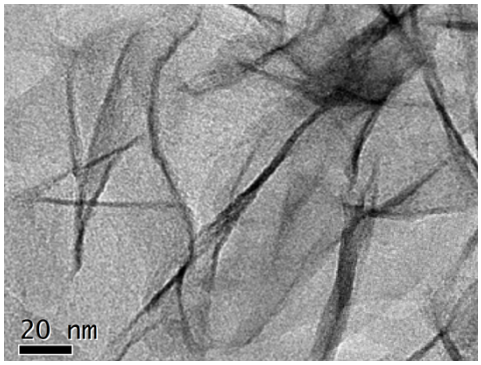

Figure S9. TEM image of the interconnected NiO/Ni layers assembled on the surface of graphene sheets.

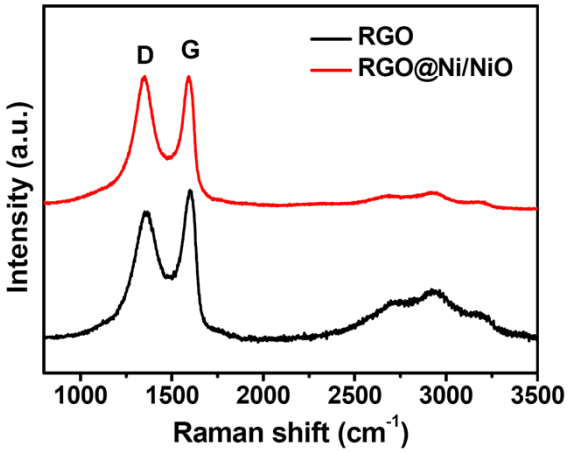

Figure S10. Raman spectra of RGO@NiO/Ni and RGO.

Figure S10 shows the Raman spectra of RGO@NiO/Ni and RGO (after the removal of ZnO). The curves presents two featured Raman shifts of carbon, the G-band at 1590 cm^{-1} is associated with the E_{2g} mode of graphitic carbon (sp^2 carbon atoms), while the D-band located at 1352 cm^{-1} corresponds to the defect induced mode. A typical feature of Raman spectrum for the RGO is that the intensity ratio of the two bands (I_D/I_G) decreases to a relatively low value (I_D/I_G=0.94, the bottom one in the Figure S10), since the carbon network will be less disordered with fewer oxygen-containing groups. It is obvious that the I_D/I_G ratio of RGO@NiO/Ni (I_D/I_G=1.23) is higher than that of RGO, resulting from the possible affection of NiO/Ni hybrids on the conjugated structures of the RGO.

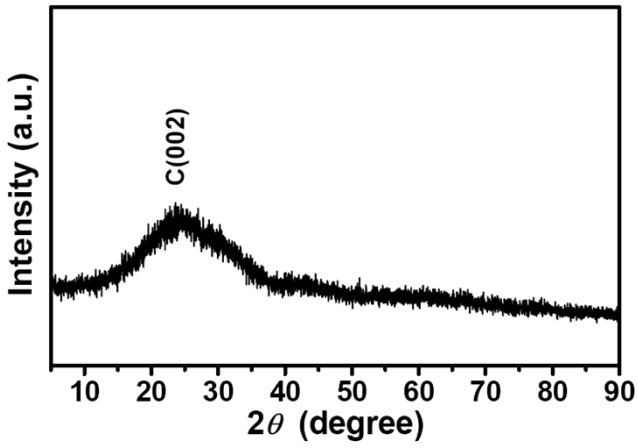

Figure S11. XRD pattern of RGO.

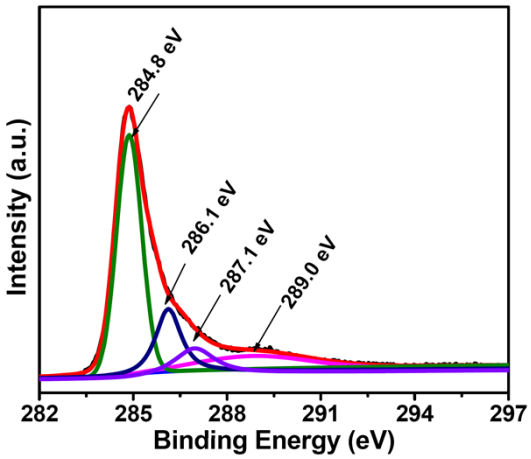

Figure S12. The high-resolution spectrum C 1s XPS peak of RGO@NiO/Ni.

The high resolution C1s spectrum (Figure S12) reveals four types of carbon bonds: "C=C/C–C" (ca. 284.8 eV), "C–O" (hydroxyl and epoxy, ca. 286.1 eV), "C=O" (carbonyl, 287.1 eV) and "O–C=O" (carboxyl, ca. 289.0 eV). For the final RGO@NiO/Ni sample, the C/O atomic ratio of RGO is ca. 8.9; the majority of oxygen functional groups have been removed and the "C–C" bonds become dominant, indicating that oxygen containing groups on RGO have been removed significantly.

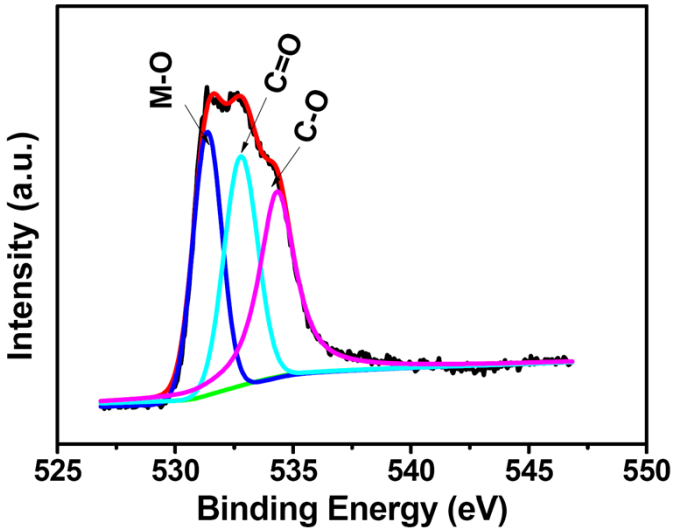

Figure S13. The high-resolution spectrum of O 1s XPS peak in RGO@NiO/Ni.

For O1s region, three energy binds are detected (Figure S13). They are 534.2, 532.8, and 531.3 eV, respectively. The main peak referenced to O1s is at 531.3 eV, which may be most likely due to the formation of the O metal binds (Ni-O).[s1]

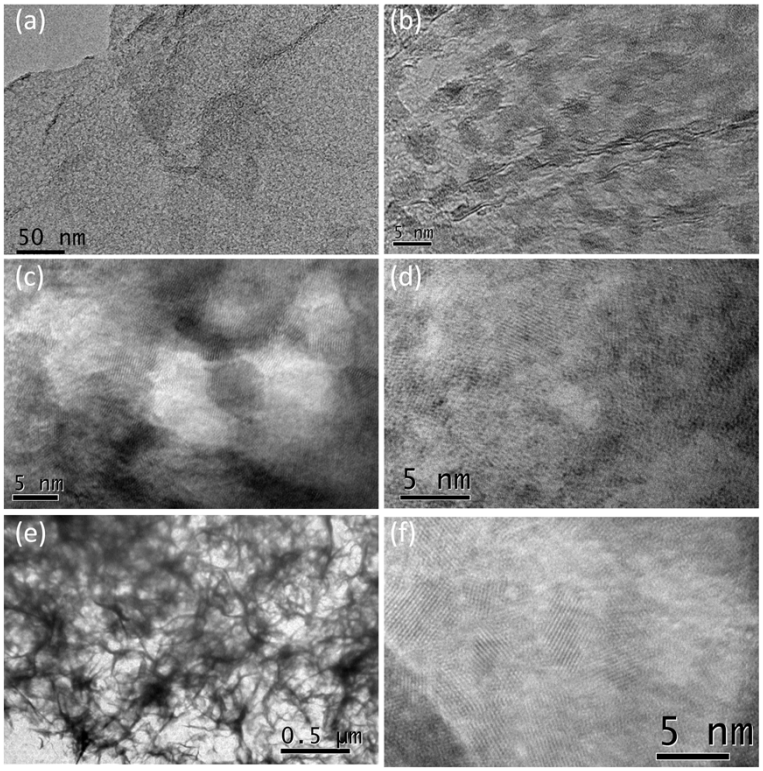

Figure S14. The samples of RGO@NiO/Ni underwent the different reaction time. (a, b) TEM and HR-TEM images of the RGO@NiO/Ni-2 after treating with NaOH solution, (c, d) HR-TEM images of RGO@NiO/Ni-5 and RGO@NiO/Ni-10. (e, f) TEM and HR-TEM images of the RGO@NiO/Ni-30.

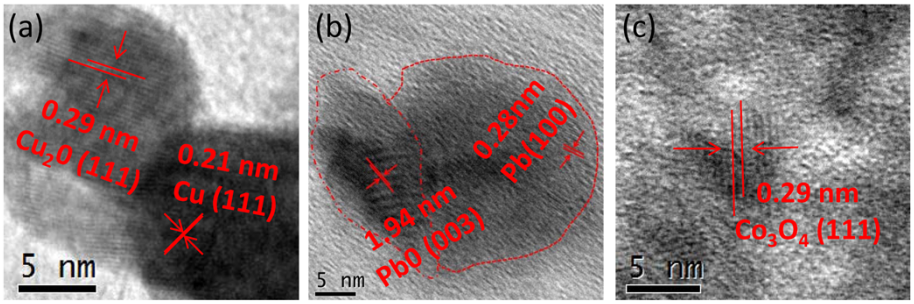

Figure S15. HR-TEM images of the 3D graphene supported Cu/Cu_2O, Pb/PbO, Co_3O_4 nanocrystallines. The interplanar spacing displayed in the images indicates the formation of the corresponding metals or metal oxides on the graphene.

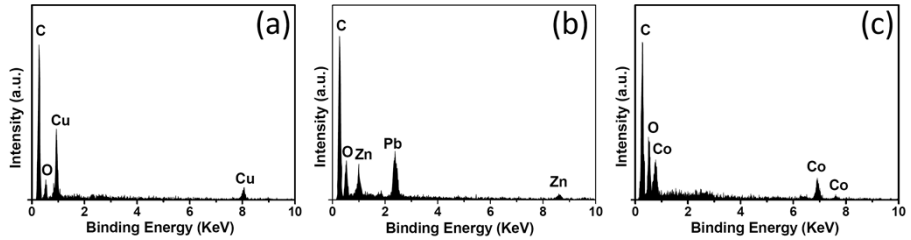

Figure S16. EDSs of $Cu\text{-}Cu_2O/RGO$, $Pb\text{-}PbO/RGO$ and Co_3O_4/RGO, respectively.

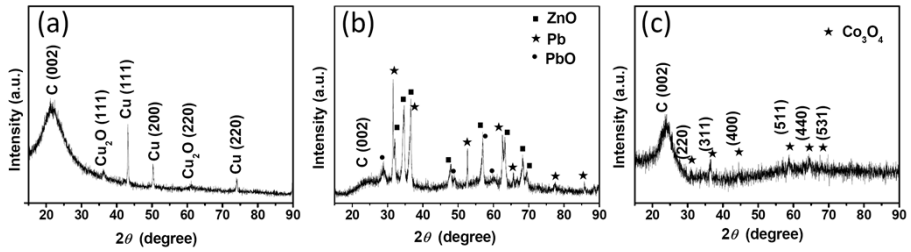

Figure S17. XRD patterns of Cu-Cu_2O/RGO, Pb-PbO/RGO and Co_3O_4/RGO, respectively.

The EDSs and XRD patterns shows 3D RGO supported single metals, metal and metal oxide hybrids, metal oxides of active metals, alloy materials etc. *via* the DSARA process. It is worth mentioning that the ZnO particles were different to remove completely from resulting samples of Cd/RGO and Pb-PbO/RGO. When the excessive washing was introduced, the Cd and Pb-PbO species were also disappeared. A better method is still under explored for the Cd/RGO and Pb-PbO/RGO samples without ZnO.

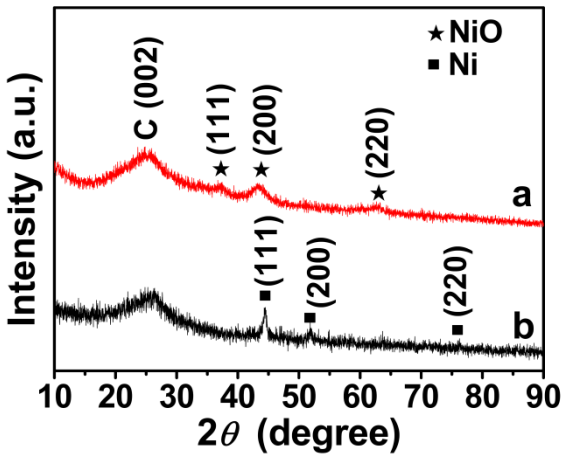

Figure S18. (a) XRD pattern of NiO species on RGO (NiO/RGO): the obtained RGO@NiO/Ni sample after being heated to 300 ºC in air atmosphere for 0.5 h. (b) XRD pattern of Ni species on RGO (Ni/RGO): the RGO@NiO/Ni sample undergoes the same experimental conditionswith Ar/H_2 atmosphere as reducing gas in the system.

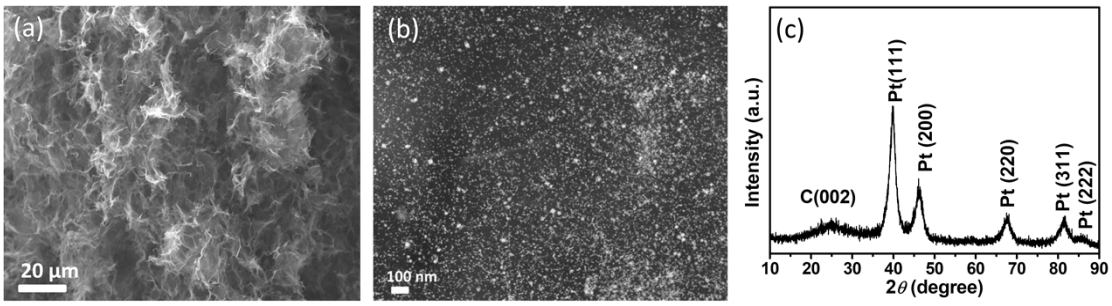

Figure S19. (a, b) SEM images at different magnifications of Pt/RGO by adjusting the initial H_2PtCl_6 solution with the concentration of Pt ions is 0.2 mg/mL; and the distribution of the Pt nanoparticles was denser than that in solution with 0.04 mg/mL Pt ions under the same reaction time.

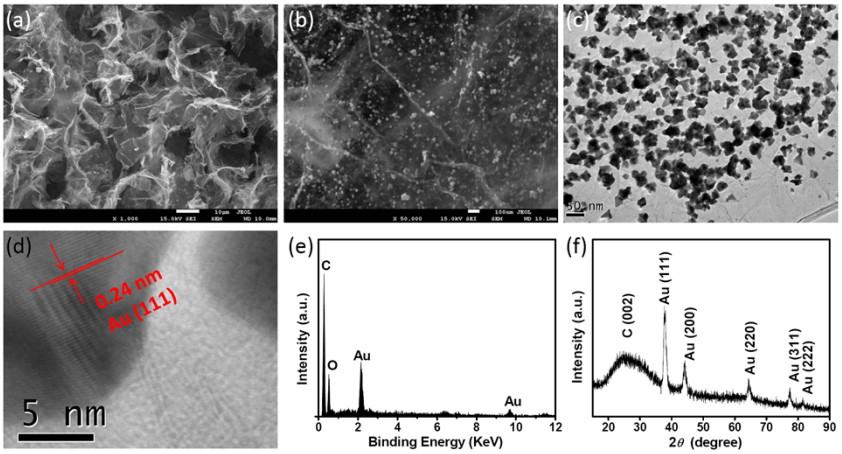

Figure S20. (a, b) SEM images of Au/3DRGO-Fe drived from Fe substrate (Fe foil) at different magnifications. (c) TEM image of Au/3DRGO-Fe. (d) HR-TEM image of Au nanoparticle. (e) EDS of the Au/3DRGO-Fe. (f) XRD spectrum of Au/3DRGO-Fe.

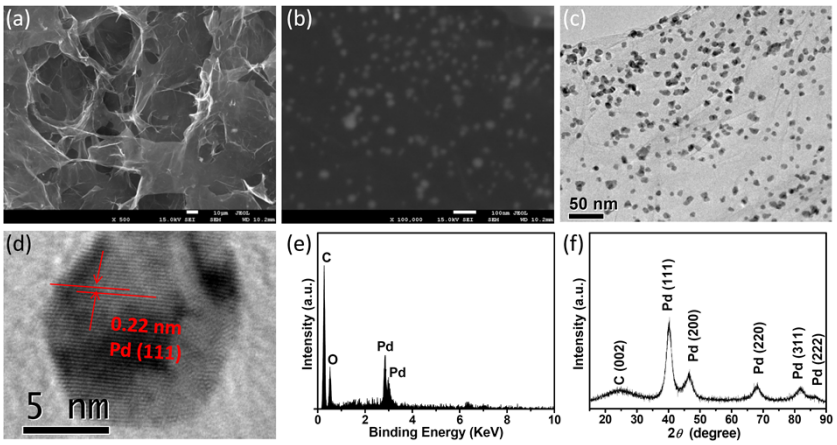

Figure S21. (a, b) SEM images of Pd/3DRGO-Cu derived from Cu substrate at different magnifications. (c) TEM image of Pd/3DRGO-Cu. (d) HR-TEM image of Au nanoparticle. (e) EDS of the Pd/3DRGO-Cu. (f) XRD spectrum of Pd/3DRGO-Cu.

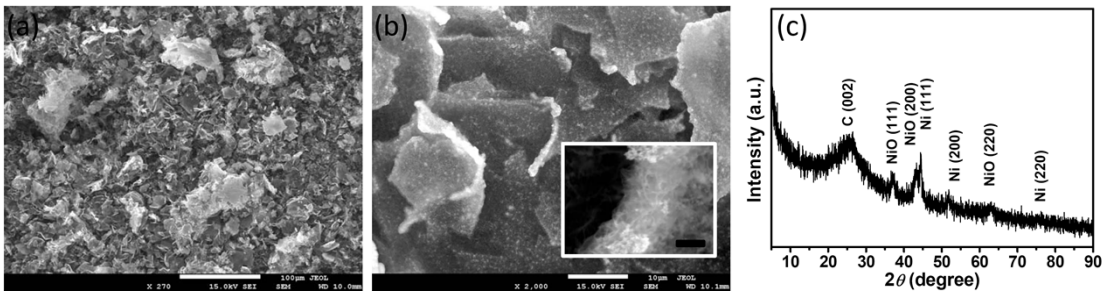

Figure S22. (a, b) SEM images of RGO@NiO/Ni after 100 cycles of discharge and charge at a current density of 0.1 A g^{-1}, and the inset in (b) is the enlargement image on the side view of the sheet. (c) The corresponding XRD pattern. The scale bar in the insert in (b) is 100 nm. Apart from the electrolyte and conductive carbon black within the sample, little change was found in the composition and structure of RGO@NiO/Ni after 100 cycling performance.

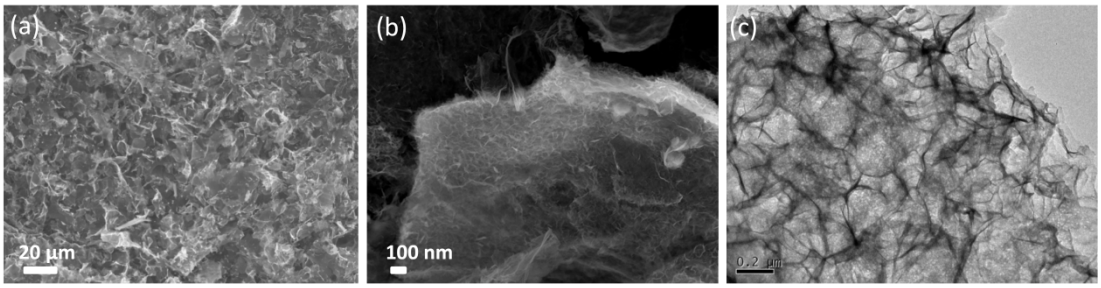

Figure S23. (a, b) SEM images of RGO@NiO/Ni after 2000 cycles of discharge and charge at a current density of 20 A g^{-1}. (c) The corresponding TEM image. The structure and morphology of RGO@NiO/Ni were well maintained as starting material. Note: With the long-time electrochemical test, the electrode should be pretreated before the SEM and TEM measurements. The cells were disassembled in the glove box after 2000 charge-discharge cycles and the composite electrodes containing the active material was recovered and washed thoroughly with the solvent, diethyl carbonate (DEC) to remove the electrolyte. Then the sample was further washed with ethanol and methanol over 3 times to remove residual Li_2O. Finally, lyophilization was applied to yield the drying sample.

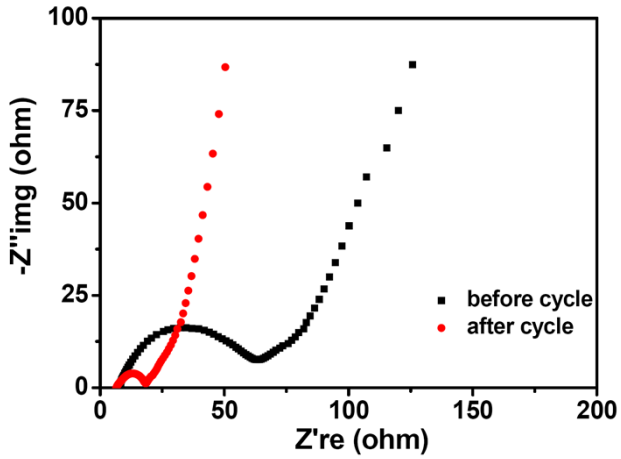

Figure S24. Electrochemical impedance spectroscopy of the coin battery (RGO@NiO/Ni) before (red) and after (black) cycling at 0.1 A g^{-1} for 100 cycles.

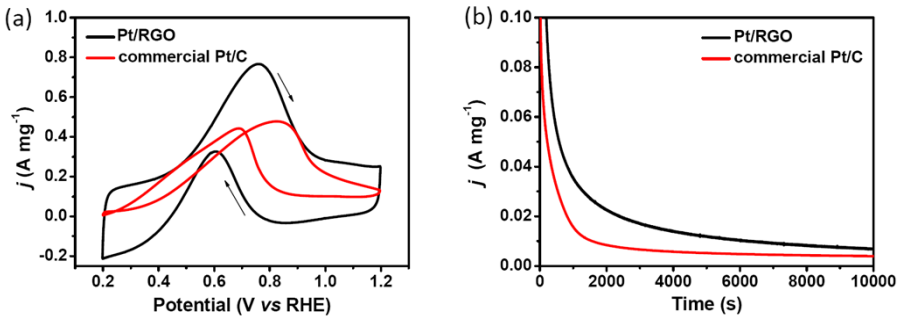

Figure S25. (a) CVs of the Pt/3DRGO and commercial 20% Pt/C catalysts in 1 M CH_3CH_2OH + 1 M KOH aqueous solution. (b) The chronoamperometric curves of the Pt/3DRGO and commercial 20% Pt/C catalysts in 1 M CH_3CH_2OH + 1 M KOH aqueous solution at a given potential of +0.7 V (*vs.* RHE).

The electrochemical measurements were conducted in a three-electrode cell by using a CHI760D electrochemical workstation. The preparation process of the electrodes as those for ORR described in the manuscript. The activity evaluation of electrocatalysts for the ethanol oxidation reaction was carried out in a nitrogen-saturated 1 M KOH electrolyte containing 1 M CH_3CH_2OH. Cyclic voltammetry curves were recorded by applying a linear potential scan at a sweep rate of 50 mV s^{-1}. The cycling was repeated until a reproducible CV curve was obtained before the measurement curves were recorded.

To evaluate the catalytic activity of Pt/3DRGO, we investigated the electrooxidation reaction of ethanol in basic medium. Ethanol oxidation is characterized by separated anodic peaks in the forward and reverse scans of the CVs. Thus, the magnitude of the anodic peak current density (j) in the forward scan is also directly proportional to the amount of ethanol oxidized at the catalyst electrodes.[s2,s3] We have evaluated the activity of PtPd/3DRGO on the basis of the total mass of active metals. As shown in Figure S25a, the activities of both the catalysts are normalized to the total mass of Pt for the comparison. The peak current density in activity per unit mass of Pt is 0.78 A mg^{-1} for the reaction on Pt/RGO electrode, which is nearly much higher than that on the commercial Pt/C electrode (0.49 A mg^{-1}). The high anodic peak current for the ethanol electrooxidation reaction on the Pt/3DRGO electrode illustrates it has superb electrocatalytic activity for direct ethanol fuel cells. Additionally, it is well known that the ratio of the forward anodic peak current (I_f) to the backward anodic peak current (I_b), I_f/I_b, could be used to describe the catalyst tolerance to incompletely oxidized species.[s4,s5] The I_f/I_b of Pt/3DRGO is higher than that of commercial Pt/C catalyst, indicating its better tolerance to the intermediate species during the oxidation reaction.

The electrochemical stability of Pt on 3D RGO, and 20% Pt/C electrodes for ethanol electrooxidation was investigated by chronoamperometric experiments at a given potential of +0.7 V (*vs.* RHE). As shown in Figure S25b, the polarization current for the ethanol electrooxidation reaction shows a rapid decay in the initial period for both of the samples, which is probably due to the formation of the

intermediate species during the ethanol electrooxidation reaction. Nevertheless, the Pt/3DRGO catalyst has much higher anodic current, and significantly slower current decay than that on the commercial Pt/C electrocatalyst. The results show that the Pt nanoparticles on 3D RGO synthesized *via* DSARA process have long-term high catalytic activity for the ethanol electrooxidation reaction. Therefore, the Pt/3DRGO has the potential application for the electrooxidation of ethanol in alkaline media.

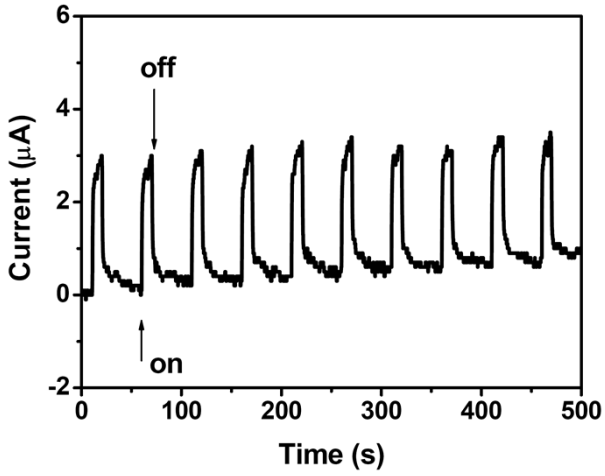

Figure S26. Photocurrent response. A typical photocurrent response for the as-prepared RGO@NiO/Ni before treating with NaOH solution, upon exposure to on/off light at room temperature. The tested sample with a length of 1 cm and a width of 0.5 cm.

The photocurrent response of the as-prepared RGO@NiO/Ni with particles was measured by applying a bias of 0.1 V to the ZnO/RGO film, while the current was recorded by CHI 760D electrochemical workstation upon exposure to a daylight lamp (100 W). The sample exhibits a fast photocurrent pulse with good repeatability (Figure S26).

Table S1. Comparison of the capacity for different carbon-based samples as anodes.

Sample	**Current density ($A\ g^{-1}$)**	**Capacity ($mAh\ g^{-1}$)**	**Ref.**
RGO@NiO/Ni	0.1	1524	This work
	0.5	1356	
	6	951	
	20	415	
	45	374	

Ni/C Hierarchical Nanostructures	0.2	931	S6
	0.5	533	
	1	356	
Ni-Sn alloy	0.298	500	S7
	3.72	200	
mesoporous NiO crystals	0.037	1237	S8
	0.37	468	
	1.49	322	
porous NiO film	0.5	490	S9
	1.5	350	
NiO-Ni composite nanoscale NiO particles	0.1	821	S10
	1	647	
porous NiO-Ni nanocomposite	0.29	387	S11
	0.71	321	
	1.14	280	
mesoporous Ni/NiO	0.1	900	S12
	1	860	
	5	750	
	10	695	
spherical NiO-C composite	0.36	430	S13
SnO_2 -Ni nanofoam	0.5	505	S14
	5	400	
	10	200	

References

S1. G. C. Li and P. G. Pickup, *J. Power Sources*, 2007, **173**, 121–129.

S2. L. Wang, Y. Nemoto and Y. Yamauchi, *J. Am. Chem. Soc.*, 2011, **133**, 9674–9677.

S3. C. Xu, H. Wang, P. Shen and S. Jiang, *Adv. Mater.*, 2007, **19**, 4256–4259.

S4. X. Yang, Q. D. Yang, J. Xu and C. S. Lee, *J. Mater. Chem.*, 2012, **22**, 8057–

8062.
S5. M. Sawangphruk, A. Krittayavathananon and N. Chinwipas, *J. Mater. Chem. A*, 2013, **1**, 1030–1034.
S6. L. W. Su, Z. Zhou and P. W. Shen, *J. Phys. Chem. C*, 2012, **116**, 23974–23980.
S7. J. Hassoun, S. Panero, P. Simon, P. L. Taberna and B. Scrosati, *Adv. Mater.*, 2007, **19**, 1632–1635.
S8. D. W. Su, M. Ford and G. X. Wang, *Sci. Rep.*, 2012, **2**, 924–930.
S9. X. H. Huang, J. P. Tu, X. H. Xia, X. L. Wang, J. Y. Xiang, L. Zhang and Y. Zhou, *J. Power Sources*, 2009, **188**, 588–591.
S10. X. H. Huang, J. P. Tu, B. Zhang, C. Q. Zhang, Y. Li, Y. F. Yuan and H. M. Wu, *J. Power Sources*, 2006, **161**, 541–544.
S11. X. F. Li, A. Dhanabalan and C. L. Wang, *J. Power Sources*, 2011, **196**, 9625–9630.
S12. E. Hosono, S. Fujihara, I. Honma and H. S. Zhou, *Electrochem. Commun.*, 2006, **8**, 284–288.
S13. X. H. Huang, J. P. Tu, C. Q. Zhang, X. T. Chen, Y. F. Yuan and H. M. Wu, *Electrochim. Acta*, 2007, **52**, 4177–4181.
S14. J. M. Haag, G. Pattanaik and M. F. Durstock, *Adv. Mater.*, 2013, **25**, 3238–3243.